WILEY | Hindawi

Research Article

Research on Internal Structure and Mechanism of Landslide Based on Hydrogeophysical Investigation (Quan'an Landslide, Southwest China)

Xiangpeng Wang,[1] Xuben Wang,[1] Kunpeng Wang,[1] Wei Luo,[2] Junqiu Xiao,[3] Jin Hu,[4,5] and Depan Hu[1]

[1]*College of Geophysics, Chengdu University of Technology, 610059, China*
[2]*Sichuan Metallurgical Geological Survey and Design Group Co., Ltd, 610051, China*
[3]*Electromechanic Engineering College, Chengdu University of Technology, 610059, China*
[4]*State Key Laboratory of Geohazard Prevention and Geoenvironment Protection, Chengdu University of Technology, 610059, China*
[5]*Sichuan College of Architecture Technology, Deyang 618000, China*

Correspondence should be addressed to Kunpeng Wang; wangkunpeng17@cdut.edu.cn

The survey area is located in the planning area of Longquan national urban park, with frequent human activities, numerous water conservancy, transportation projects, and frequent geological disasters such as landslides. The Red Mudstone has low strength and easy to soften in the case of water, and it is very prone to landslide in rainy season. At present, there are many studies on Red Mudstone Landslides, but most of them are analyzed by geological means, and the monitoring process is also dominated by surface deformation and settlement; there is less analysis with hydrogeological that is caused by rainfall and human activities. For Red Mudstone Landslides, to effectively reveal and analyze the process of the Slip Mechanism, we need to carry out the characteristics of hydrogeological structure and underground physical structure, and compare with surface monitoring and point geological structure. In this study, a one-year field survey and hydrogeophysical survey were carried out. Combined with the characteristics of environmental geology, the geophysical forward modeling problem based on finite element method was used to verify the influence of rainfall on the electrical characteristics of underground media. The smoothness constrained least square method and three-dimensional unstructured grid method are used to interpret the ERT data, analyze the abnormal patterns of electrical structure of landslide in different seasons, and correspond well with the GPR data. According to the characteristics of surface vegetation and weathering, as well as the displacement and settlement monitoring after landslide, the spatial characteristics of red bed landslide are revealed, and the relationship between landslide, rainfall, and human activities is clarified.

1. Introduction

Heavy rainstorms, continuous heavy rainfall, and earthquake are the key causes of geological disasters, such as landslides and collapses, especially in shallow landslides [1, 2]. In China, 90% of landslides are either directly or indirectly induced by rainfall [3, 4]. According to the Chinese Statistics Bureau, 527 fatal landslides in China caused 5151 deaths and economic losses of 6.7 billion yuan [5].

Such as on September 16, 2011, heavy rainfall induced large-scale mass geological disasters in Nanjiang County with 1860 disaster points in total, among which 1,162 were newly identified disaster points. Landslides accounted for more than 85% of the newly identified disaster sites [6, 7]. Hence, it is necessary to carry out close monitoring of the existing hidden danger points and analyze the geological characteristics and landslide composition characteristics of occurred landslides site and analyze the landslide

formation mechanisms from multiple aspects to reduce the damage [8]. The red bed is a Mesozoic and Cenozoic clastic sedimentary rock with red color in appearance. It is mainly continental sedimentary and mainly lithology is sandstone, mudstone, and shale. It is widely distributed in Southwest China, such as Sichuan, Shaanxi, and Gansu. The red layer is mainly composed of argillaceous rock, sandstone, and so on. Its main characteristics are low strength, easy to melt in water, notable rheology, and are easily weathering [9]. Red Mudstone Landslide occurred in China accounts for a higher proportion, especially in the southwest.

In recent decades, researchers have used different methods to analyze the relationship between various geological disasters and the respective causes from the perspective of hydrogeology and environmental geology. In previous studies, interferometric synthetic aperture radar was used to detect and quantify land subsidence caused by aquifer system compaction, which guided hydrogeological data collection of settlement surveys [10]. The rainfall-induced landslide prediction model was used to analyze the relationship between rainfall and landslide movement [11]. Electric resistivity tomography (ERT) was used to investigate and determine the distribution of waste slag accumulation and analyze the relationship between its respective distribution and collapse accidents [12]; Liu et al. [13] studied the size effect of red-bed soft rock, which needs to consider the joint effect of height-diameter ratio, Poisson's ratio, and deformation modulus. Hang et al. [14] studied the water physical characteristics of the middle Yunnan red layer and analyzed the microscopic mechanism of the expansion and dissolution of the red layer. Zhong et al. [15] conducted an experiment on the swelling variation characteristics of red-bed soft rock in Sichuan and concluded that the red-bed soft rock is nonswelling and has low water absorption and expansion rate. Zhou et al. [16, 17] discussed the main characteristics of red layer soft rock slope in South China, including the geomechanical structure and failure characteristics of the slope, and made statistics of four common failure modes. Liu et al. [13] discussed the chemical, physical, and mechanical effects of different flow regimes on the softening of red sandstone, and revealed the influence mechanism of different flow regimes on the softening of red sandstone. Zhang et al. [4] studied the disintegration and fracture evolution process of red bed soft rock, and analyzed the disintegration ratio characteristics of different mesh sizes. The dynamics model of softening interface of soft rock was established by Fick diffusion law, and the formation law of water-rock interface was well described. Xie et al. [18] carried out natural state, saturated uniaxial, and triaxial compression experiments on red bed soft rock, and analyzed the water softening mechanism of red bed soft rock. Huang et al. [19] studied on the disintegration characteristics, durability characteristics, and the synergistic effect of water and temperature in the dry-wet cycle of red-bed soft rock. Zhou et al. [20] analyzed the effect of water-rock interaction on physical, and mechanical properties of rock were analyzed by scanning electron microscopy (SEM).

Electromagnetic methods are sensitive to both groundwater and low-resistivity bodies. Therefore, they have become the key approach for disaster monitoring and environmental investigation. Additionally, electromagnetic methods are effective for frozen soil and glacier monitoring, pollution detection, engineering practices, and hydrogeological exploration [21, 22]. The research above shows that the Red Mudstone is easy to distinguish from bedrock, and the causes of Red Mudstone Landslide in different study areas are closely related to the surrounding environment [23]. In this study, rainstorm landslides were analyzed by comprehensively exploring the effects of hydrogeology, environmental geology, and post-prevention of the disaster.

The research on the relationship between secondary landslides and surrounding civil facilities during heavy rainfall in red bed soft rock area has not been fully studied. There are relatively few literatures on the analysis of landslide mechanism through long-term observation by geophysical methods. In this study, we leveraged electric resistivity tomography to identify the impact of seasonal rainwater on the electrical characteristics of underground structures. The development of underground structural fissures and the extent of the impact of groundwater were also estimated. Meanwhile, we compare and analyze the internal electrical structure of landslide in different seasons with radar detection, geological disaster monitoring, and other data. The results show that the water tables in landslide areas provide valuable information about establishing monitoring and early warning systems, which are useful for predicting the movement of translational landslides with high concealment and high risk. Therefore, it is of great research value to use resistivity method and ground penetrating radar (GPR) to carry out geological survey and forward simulation in the area of red bed soft rock.

Our field investigations and geophysical survey suggest that the study slope may fail in the future in the event of heavy rain fall and/or earthquakes. Hence, to avoid secondary disasters, it is crucial for the local government to strengthen the monitoring and early warning systems of landslides. Additionally, as rainstorms frequently cause serious casualties and economic losses worldwide, it is essential to study and evaluate the impact of rainfall and disasters resulting from human activities to guide disaster prevention.

2. Study Area Description

The study area is located in Longquan Mountain, and the hydrogeological structure of the red layer in the study area (Figure 1). In the early morning of August 17, 2020, a landslide, largely due to a rainstorm, occurred in Group 5 of Quan'an Village, Eastern New District of Chengdu, resulting in the collapse of six houses. Specifically, the length, width, buried depth, and volume of this landslide were approximately 210 m, 180 m, 35 m, and $13.23 \, m \times 105 \, m^3$, respectively. At present, investigation and follow-up monitoring have been carried out. One year after the landslide, many surface plants died, and due to timely warnings and the relocation of villagers to safe areas, no deaths or injuries occurred. However, multiple secondary disasters were
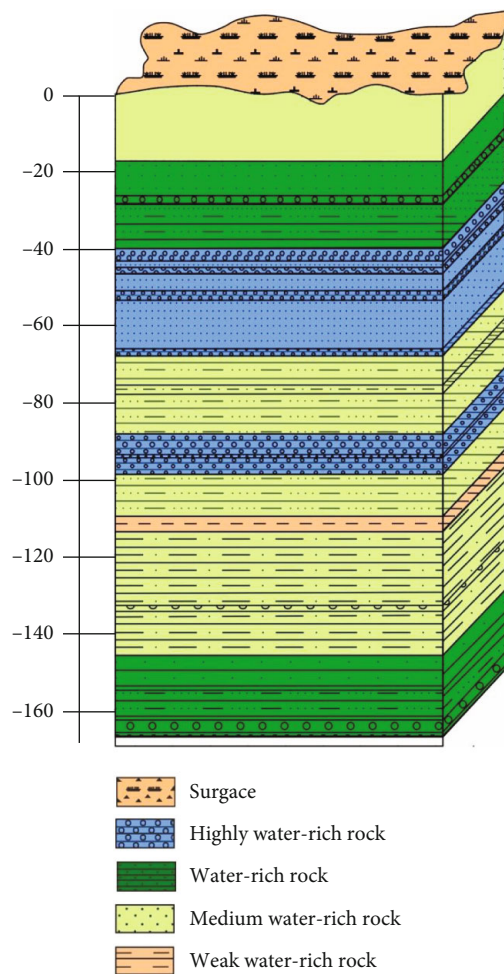
FIGURE 1: The hydrogeological structure in the study area [23].

Legend:
- Surgace
- Highly water-rich rock
- Water-rich rock
- Medium water-rich rock
- Weak water-rich rock

caused by rainstorms, including additional landslides and collapses in Quan'an Village, resulting in damaged farmland, roads, and houses.

The area has a subtropical humid monsoon climate [24], with four distinct seasons. Sandstone forms a permeable layer, the mudstone is relatively water-resistant, and the contact zone between the two is made up of a highly water-saturated zone [25]. Studies have revealed that the presence of stagnant water in the residual soil layer and the increase in pore water pressure were the main reasons for rainfall-induced landslides [26]. The geological structure of Longquan Mountain is predominantly composed of a soft rock "red layer." Therefore, the landslides occurring within the incident area were low-strength Red Mudstone Landslides.

Based on this, our study reconsidered the relationship between the stability of the soil and the characteristics of the "red layer." Previous research on the characteristics of Red Mudstone and soil stability focuses more on the physical characteristics of mudstone. Han et al. focused on the time effect of the long-term interaction between mudstone and water in the "red layer" area and further explored the rate of mudding and rock softening by analyzing samples from reservoirs built at different times in the Longquan area as well as saturated rock samples in the reservoir area [27].

Through field inspections of 16 reservoir sampling points in Sichuan and laboratory microanalysis and measurement of collected rock samples, Han et al. [28]. revealed that the softening coefficient of the "red layer" gradually decreased with age after long-term immersion.

2.1. Geological Setting. The "red layers" are clastic sedimentary rocks dominated by red continental sediments, which are widely distributed in Southwest China. The lithology is primarily comprised of sandstone, mudstone, siltstone, and shale. This kind of landslide is the most widely distributed and has the greatest environmental impact in China. It covers Sichuan, Yunnan, Guizhou, and other provinces, and the research is of great significance. The "red layer" has poor compression strength, shear resistance, and low mechanical strength [29]. The long-term interaction between mudstone and water results in a significant change in its physical and mechanical properties, leading to the argillization and softening of the mudstone, leading to landslide disasters occur frequently and endanger the safety of the surrounding environment. Additionally, the shear strength of the rock mass decreased sharply [30]. Other characteristics include strong hydrophilicity and poor water permeability (Li (2017)) [31]. The presence of red beds allowed the overlying slope to slide along a gently inclined layer during the rainy season [32]. Under specific physical and chemical conditions, the low-strength plastic soil, soft plastic soil, flowing plastic rock, and soil mass that are created in the sliding zone are a key part of landslides. The aforementioned factors impact the development, deformation, and stability of landslides (Li (2017) [33]; Hungr et al. (2014)). With increasing depth, the gypsum content in Red Mudstone increases. Under the action of acidic environmental water, soluble components in Red Mudstone gradually dissolve, resulting in larger pores and stronger permeability [25].

Figure 2 shows the process of surface fissure development within the landslide mass, with substantial weathering evident throughout the "red layer." Surface fissures were formed in different directions, which predominantly caused the occurrence of landslides twice, in different directions. After a landslide, the rock stratum at the crack was exposed. After erosion during the rainy season and a freeze–thaw cycle in winter, the rock stratum weathered further and broke down. S2 shows a relatively complete rock section, whereas S3 and S1 show broken sections. S3 was developed from the same layer as S1. This highlights various characteristics of the "red layer," including softening in water and poor freeze–thaw resistance (poor freeze-thaw resistance accelerates rock fragmentation, reduces rock strength, and finally makes landslide easier to occur).

2.2. Rainfall. The Sichuan Climate Center records indicate that the flood season in Sichuan during 2020 was from May to September. However, extreme weather events were more likely to occur due to unpredictable spatial changes and alterations between droughts and floods [34–36]. In midsummer (July to August), floods in the south and southwest of the basin tend to be heavy. During this time, the

FIGURE 2: Landslide area surface photographed in different seasons. The picture on the left was taken on September 1, 2020. The picture on the right was taken on March 2, 2021. L represents the almost north–south fracture, F represents the almost east–west fracture, and S represents weathered red-bed soft rock.

TABLE 1: Daily rainfall data (average) of the observatory from August 4 to 24, 2020.

Data	8.4	8.5	8.6	8.7	8.8	8.9	8.10
Rainfall (inch)	0.15	0.01	1.77	0.10	0.11	0.00	0.01
Data	8.11	8.12	8.13	8.14	8.15	8.16	8.17
Rainfall (inch)	9.11	1.78	0.01	1.42	2.47	5.87	2.16
Data	8.18	8.19	8.20	8.21	8.22	8.23	8.24
Rainfall (inch)	0.14	0.01	0.00	0.00	0.81	0.31	0.03

periods of intense precipitation in the Longmen Mountains, peripheral mountains, and Panxi region typically result in flash floods and mudslides.

Danjing Mountain is located in the middle of the Longquan Mountains. It borders Shuangliu County, Chengdu City and Renshou County, Meishan City, and has a maximum height of 974 m. According to statistics, in 2020, there were 117 days of rainfall throughout the year, with 13, 18, and 16 days of rainfall in June, July, and August, respectively. The total average annual rainfall in Chengdu is 590–610 mm. The strata in the landslide area are predominantly comprised of highly weathered sandstone, mudstone, and loosely consolidated soil. In the event of rainstorms, the rock and soil became saturated with rainwater, making the slopes extremely vulnerable to repeated slope failures [35]. According to the records of the observation station closest to the landslide, rainfall began increasing sharply from August 11, 2020, with 9.11 cm of rainfall reported on 11 August 2020.

Finally, a landslide occurred on August 17, 2020. The daily rainfall data of the observatory from August 4, 2020, to August 24, 2020, are shown in Table 1, and the position of rain gauge is shown in ① ② ③ in Figure 3.

The above monitoring data were obtained from the surface rain gauge of the geological disaster monitoring points within the scenic area (the data were provided by the Geological Environmental Monitoring Institute in Chengdu) and have been used to indicate the surface rainfall in the study area. Evidently, heavy rainfall occurred from June to September 2020 (Figure 4). The monitoring results of the surface rain gauge were consistent with the rainfall statistics of the meteorological department. The sudden increase in rainfall over a relatively short period led to a rapid rise in the groundwater level, water immersion softening of red-bed soft rock, and an increase in the lateral stress of the sliding mass, which directly resulted in the occurrence of landslides.

2.3. Human Activity. As shown in Figure 5, a highway crossed the front edge of the landslide, forming an overhead strong stress load zone (the yellow solid line in the figure is shown). Due to road-related construction activities, the distribution of the slope rock mass was changed, leading to increased erosion and changes in groundwater movement [37, 38]. The middle area of the slope was cultivated land and economic crop forest. The southeast corner of the slope was occupied by various factory buildings. Five houses and artificial reservoirs were distributed throughout the northern and southeastern corners of the slope (① in the figure). The degree of damage to surface vegetation and subsequent

FIGURE 3: Aerial photo taken by drone. The yellow dotted line indicates the secondary landslide caused by pool collapse, and the red arrow indicates the sliding direction of landslide.
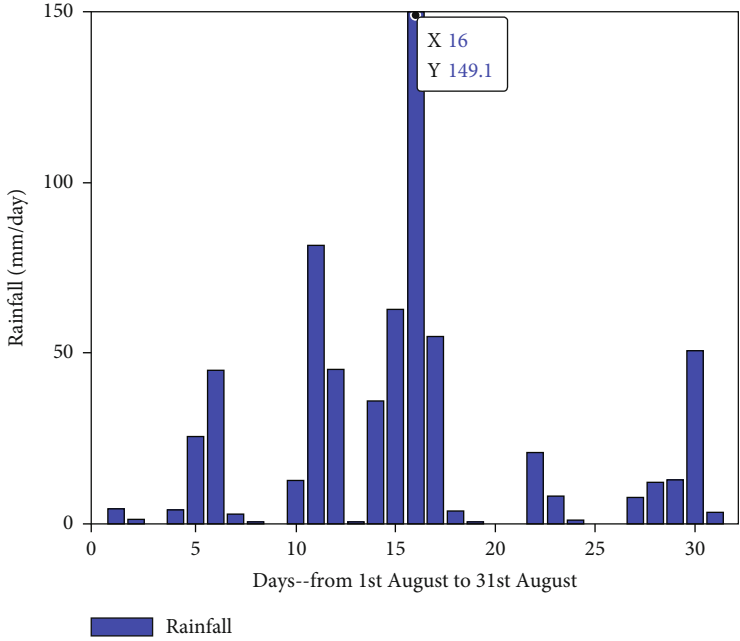

FIGURE 4: The precipitation data provided by Geoenvironment Monitoring Institute in Chengdu.

FIGURE 5: Satellite image before the landslide. The red dotted line indicates the area of the first landslide and the second landslide. The yellow dotted line indicates the entire study area.
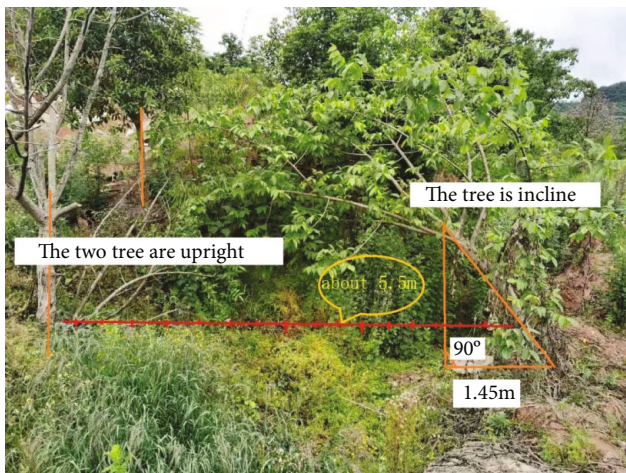

FIGURE 6: Vegetation indicating the occurrence of the secondary landslide. Trees on the left and right sides were approximately 4.2 m apart. Vegetation on the right side was affected by the secondary sliding body, and vegetation on the left side was affected by the primary sliding body but not by the secondary sliding body.

restoration thereof were linked to soil erosion and groundwater conservation Liu et al. [39]. The formation of shallow landslides, or debris flows, is influenced by the characteristics and make-up of local vegetation (Li et al. (2021)). The studied landslide had a fracture zone along the back edge, with a house and factory located along it (② in the figure). The front edge crossed the highway, and an artificial reservoir was located at the back edge of the secondary landslide.

The direction of the secondary landslide was from the artificial reservoir to the houses.

3. Investigation and Analysis

3.1. Formation Mechanism. Landslides are a natural disaster resulting from rainfall, specific lithological characteristics, human activities, earthquakes, hydrology, and other conditions [9, 40–44]. In the "red layer" area, landslides can be divided into low soil strength landslides and high rock strength landslides [45, 46]. Therefore, the study landslide was considered a low soil strength landslide based on the inclination angle and a thick-layer landslide based on the development pattern [47].

The landslide body, along with the secondary landslide, was extremely large (the slope range is shown in Figure 3). The first slip occurred on the southeast side, and its distance was approximately 11.2 m. As shown in Figure 3, after the initial landslide, the geological body was loosened. A further increase in rainfall resulted in increased water within the artificial pool (red dotted line area), and the cracks in the pool that were caused by the first slip further increased. This led to the collapse of the pool and resulted in the second landslide (yellow dotted line area in Figure 3). The impact of the secondary landslide on surface vegetation can be clearly observed in Figure 6. Specifically, the trees on the left side of the image are not inclined, whereas the trees on the right side are substantially inclined. As the trees had grown along the back edge of the artificial pool, the positioning of the trees indicates that trees on the right side of the image were affected by the secondary sliding mass, whereas the
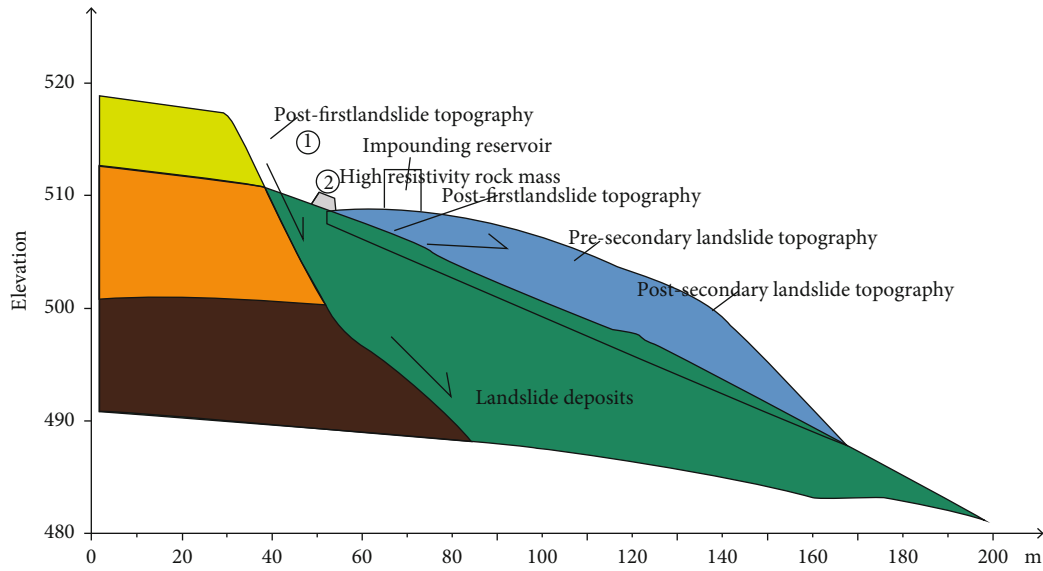
FIGURE 7: Landslide pattern, showing the west–east section of the landslide. The ordinate indicates the altitude, abscissa indicates the horizontal distance of the landslide, arrow indicates the slip direction, and different colors represent different strata information. ① indicates the trailing edge of the landslide mass, and ② indicates a hard rock mass within the landslide mass. Vegetation here is not inclined.

FIGURE 8: Fault zone at the back edge of the landslide. The trailing edge of the collapse zone extends from north to southwest, with a maximum depth of 6 m and a total length of approximately 210 m.

trees on the left side of the image were affected by the primary sliding mass but not by the secondary sliding mass. The field survey revealed that the trees on the right side of the image were approximately 3.6 m from the artificial pool. The straight-line distance between the trees on the left and right sides was approximately 4.2 m. The slope development and vegetation were similar to those indicated by the arrows in Figure 3.

The surface vegetation and direction of the slope cracks shown in the aerial photograph indicate the overall shape of the landslide. As shown in Figure 6, the first landslide occurred on the southeastern side of the slope, whereas the

secondary landslide occurred on the eastern slope. The two landslides were related. Secondary landslides occur after the primary landslide and have a different volume and surface exposure compared to the primary landslide. The box in Figure 7 represents the location of the artificial reservoir. The continuous rainfall led to an expansion of the fissures at the trailing edge of the sliding body, and finally, tensile collapse occurred. Figure 8 shows the fracture of the trailing edge of the slope.

3.2. Effects. Landslides have a substantial impact on the surrounding environment [48], an example of which can be
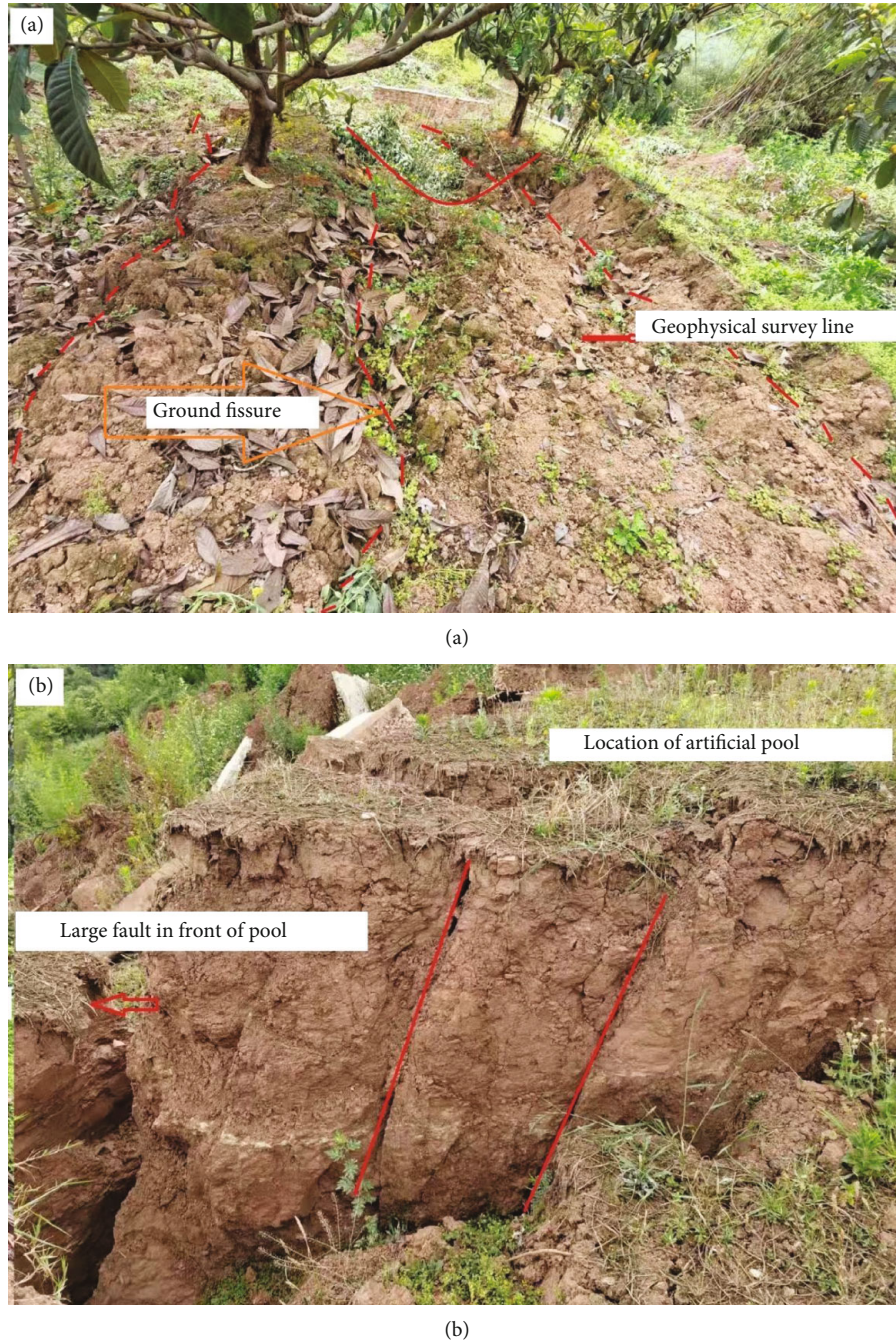
(a)

(b)

FIGURE 9: Land subsidence and cracks. (a) A large number of settlement and fissure areas throughout the loquat forest land on the northeast side of the landslide. (b) An inclined fissure at the bottom of the reservoir.

observed in Figure 9. On the northeast side of the sliding mass, a large number of settlement and fracture areas appeared in the loquat plum forests, with the widths and lengths of the fractures ranged from 2 to 19 cm and from 1.2 to 13.0 m, respectively. The minimum and maximum diameters of the irregular settlement areas were 40 cm and 2.3 m, respectively. As shown on the right-hand side of Figure 9, a large eastward fracture collapse occurred on the east side of the reservoir, and an inclined fracture appeared at the bottom of the reservoir. The fracture was approximately 1.3 m. From the vergence and collapse directions of

the fracture, it can be observed that the formation of the fracture was affected by the primary stratum slip [49]. The collapse was caused by water flow after the reservoir rupture, which is consistent with previous findings regarding the cause of the secondary landslide [50]. A large collapse zone at the rear edge of the slope is shown in Figure 8. Five houses located either at the rear edge or within 10 m of the right-hand side of the landslide.

They were destroyed by the landslide. This indicates that the construction of houses and fields with human activities had a substantial impact on the stability of the slope. With
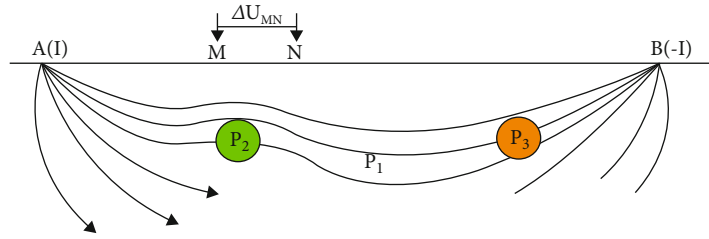
FIGURE 10: Working principle of the electric resistivity tomography. When the current propagates through underground, due to different lithology and fracture development in the underground space, the formation resistivity at different locations in the underground space is as shown by $\rho 1$, $\rho 2$, and $\rho 3$. The current density is also different, as shown in the dense and sparse distribution of current schematic lines. The resistivity value was calculated through the collected potential difference (ΔUMN), after which the geological anomaly was divided through the resistivity value to realize the spatial display of geological information.

(a) Point A is on the closed surface　　　　　　(b) Point A is out the closed surface
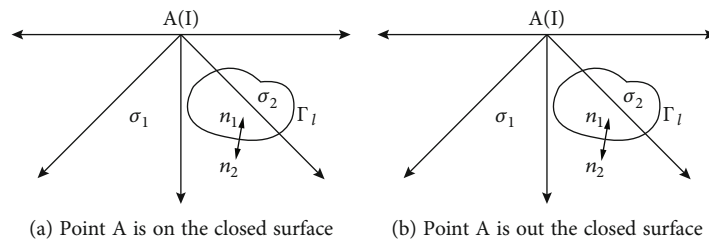
FIGURE 11: Point source 2-D electric field sketch map.

frequent human activities and changing climate extremes, it is necessary to investigate, monitor, and prevent potential landslides in a timely manner by implementing protection countermeasures in vulnerable areas.

4. Geophysical Investigation

Geophysical exploration can reflect the deep structural characteristics of landslide mass, which is conducive to the interpretation and evaluation of landslide combined with hydrogeological structural unit and surface monitoring. Firstly, the mechanical test of rock samples in the study area is carried out, and the data is used as the parameters of geophysical forward modeling to ensure the reliability of forward modeling results; secondly, the electric resistivity tomography is used to measure the study area in different seasons to reflect the changes of electrical structure characteristics of landslide caused by rainfall in different seasons; thirdly, GPR is used to measure the shallow surface to eliminate the defect of insensitive response of electric resistivity tomography to the shallow layer, and the deep electrical structure is compared at the same time; finally, compared with hydrogeological structure and surface monitoring, while determining the effectiveness of the measurement results, the three-dimensional inversion is used to carry out three-dimensional imaging of the study area to intuitively show the shape of landslide mass.

4.1. Mechanical and Electrical Conductivity Test. In this study, 14 samples were taken at different locations within the range of the landslide mass, of which sample 3 was not tested due to fragmentation. The dry sample data were obtained by testing the collected original samples, and the wet sample data were obtained by testing the samples after 24 hours of immersion in distilled water. The maximum resistivity of the dry samples was 1000 $\Omega \bullet$ m, and the minimum was 8.9 $\Omega \bullet$ m. It is feasible to study the effect of rainfall on groundwater by measuring the resistivity in different seasons and then estimate the formation of landslides triggered by rainfall.

4.2. Electric Resistivity. Electric resistivity tomography has characteristics of both electrical profiling and electrical sounding, thereby meeting the requirements of shallow fine exploration. In the exploration process, the polar distance can be changed according to the demands 190 of exploration requirements at different depths. This method has a high detection efficiency and high precision, can accommodate large volumes of data and information, and is rapid. It is a commonly used geophysical method for delineating lithologic interfaces, structural fracture zones, and underground aquifers [30, 51, 52]. The electric field characteristics of the two-point sources are shown in Figure 10. When measuring the resistivity of underground media, an electric field is supplied at two points, namely, A and B. The potential difference is measured at any M/N point to calculate the resistivity of the underground medium. High-density measuring devices can be divided into the Wenner quadrupole, Europole, and differential. This study used a quadrupole device; data were processed using Swedish RES2DINV software, and the least square method was used to calculate the terrain inversion of the geological model.
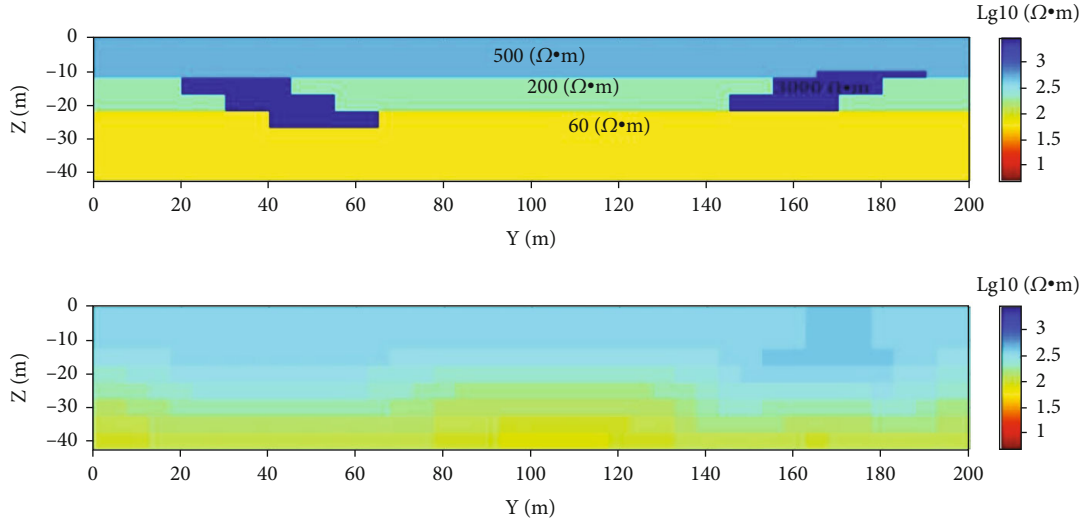
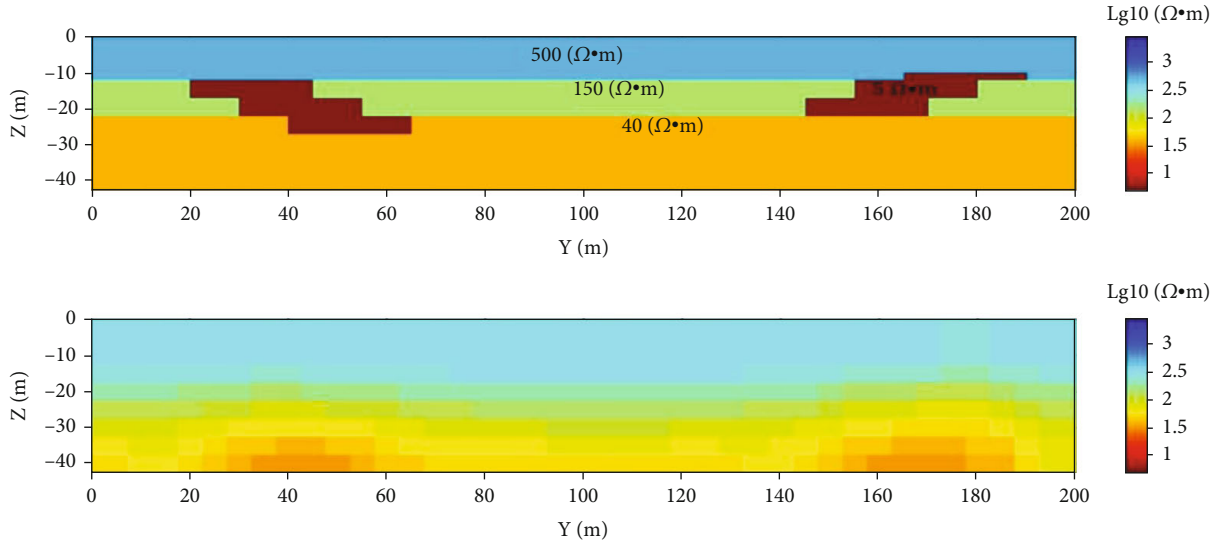FIGURE 12: Model of winter and forward simulation results.

FIGURE 13: Model of autumn and forward simulation results.

The potential difference can be expressed as follows:

$$U_M^{AB} = \frac{I\rho}{2\pi}\left(\frac{1}{AM} - \frac{1}{BM}\right),$$

$$\Delta U_{MN} = U_M^{AB} - U_N^{AB} = \frac{1\rho}{2\pi}\left(\frac{1}{AM} - \frac{1}{BM} - \frac{1}{AN} + \frac{1}{BN}\right). \tag{1}$$

The calculation formula of resistivity can be expressed as follows:

$$\rho = K\frac{\Delta U_{MN}}{I}. \tag{2}$$

4.3. Forward Simulation of Electric Resistivity Tomography.
Suppose there is a current source at point A on the surface, the current is I, and the ampere density vector is j, as shown

in Figure 11: The 2-D boundary value problem of direct current is:

$$\begin{cases} \nabla\bullet(\sigma\nabla U) - k^2\sigma U = -I\delta(A) \in \Omega \\[2mm] \dfrac{\partial U}{\partial n} = 0 \in \Gamma_S \\[2mm] \dfrac{\partial U}{\partial n} + k\dfrac{K_1(kr)}{K_0(kr)}\cos(r,n)U = 0 \in \Gamma_\infty , \\[2mm] U_1 = U_2 \in \Gamma_1 \\[2mm] \sigma_1\dfrac{\partial U_1}{\partial n_1} = -\partial_2\dfrac{\partial U_2}{\partial n_2} \in \Gamma_1 \end{cases} \tag{3}$$

where σ is the conductivity, k is the parameter in the wavenumber domain, U is the potential in the wavenumber domain, and I is the supply current. $\delta(A)$ is the location of
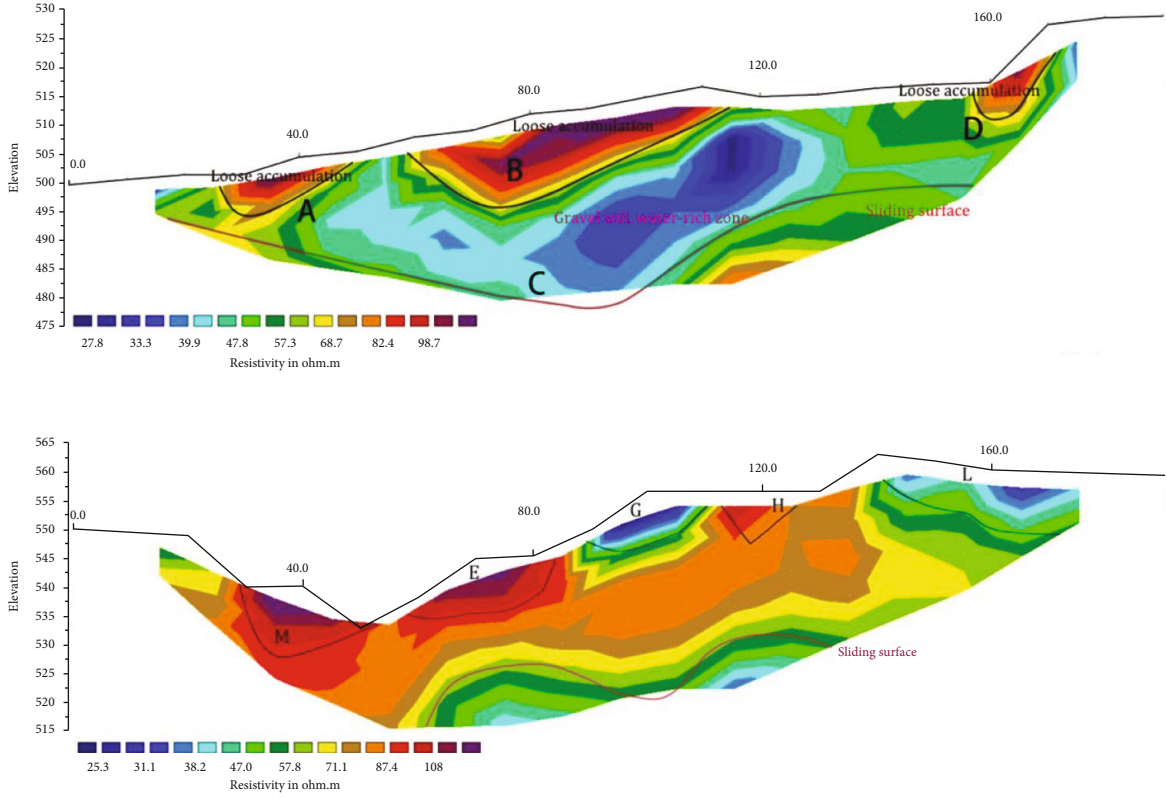
FIGURE 14: Measurement results in spring.

power supply point (A), $\partial U/\partial n$ external normal of potential to surface boundary in wavenumber domain, K_0 is the second kind of zero order revise Bessel function, K_1 is the second kind of single order revised Bessel function, $\cos(r, n)$ is the cosine of the angle between the radius vector from point A to the boundary point on the boundary and the external normal direction n of the point [7].

In this paper, we use the weighted residual method to solve the boundary value problem. The corresponding variational problem is:

$$
\begin{cases}
F(U) = \int_\Omega \left[\dfrac{\sigma}{2}(\nabla U)^2 + \right. \\
\dfrac{1}{2}K^2\sigma U^2 - I\delta(A)U d\Omega + \dfrac{1}{2}\int_{\Gamma_\infty} \sigma \dfrac{kK_1(kr)}{K_0(kr)}\cos(r,n)U^2 d\Gamma \\
\delta F(U) = 0
\end{cases}
\tag{4}
$$

When we use the abnormal potential method, the corresponding variational problem is:

$$
\begin{cases}
F(U) = \int_\Omega \left[\dfrac{\sigma}{2}(\nabla U)^2 + \right. \\
\dfrac{1}{2}K^2\sigma U^2 + \sigma \nabla U_0 \bullet \nabla U + \sigma' K^2 U_0 U d\Omega + \\
\int_{\Gamma_\infty} \left[\dfrac{1}{2}\sigma \dfrac{kK_1(kr)}{K_0(kr)}\cos(r,n)U^2 + \sigma' \dfrac{kK_1(kr)}{K_0(kr)}\cos(r,n)U_0 U \right] d\Gamma \\
\delta F(U) = 0
\end{cases}
\tag{5}
$$

where U_0 is the normal potential when the background conductivity is $\sigma 0$ under the condition of a uniform half space, σ is the conductivity of underground, σ' is the underground abnormal conductivity ($\sigma'' = \sigma' - \sigma' 0$), and U is the abnormal potential, after solving, the total potential is $V = U + U0$.

In this study, both methods were used to achieve the final results. In the case of undulating terrain conditions, the normal potential at the grid nodes could not be obtained via simple analytical calculations, and hence, only the total field potential method could be used. When simulating the horizontal terrain, the results of the total field potential method and abnormal field potential method were separated only at the node closest to the source. Thus, the abnormal potential method was used to improve the accuracy of the solution. In this study, the rectangle was divided into two triangular elements. The forward simulation used a symmetrical quadrupole device; the polar distance was set to 5 m, and the number of electrodes was 41.

From the simulation results (see Figures 12 and 13), it can be seen that electric resistivity tomography can better describe the location and spatial range of the abnormal body. It can describe the interface of the rock layers based on the different resistivities in the underground space and sensitively describe the change in water content in the underground medium. This can highlight the existence of low-resistivity anomalies and is conducive to the investigation and follow-up evaluation of landslide disasters caused by heavy rainfall.
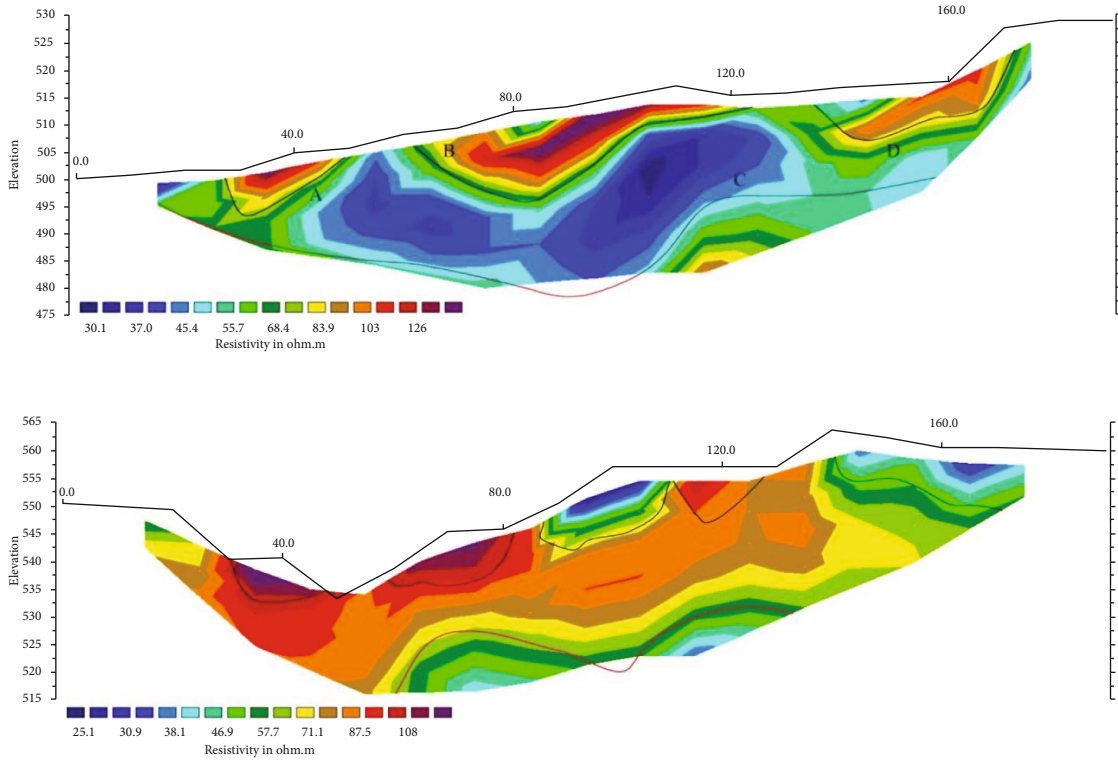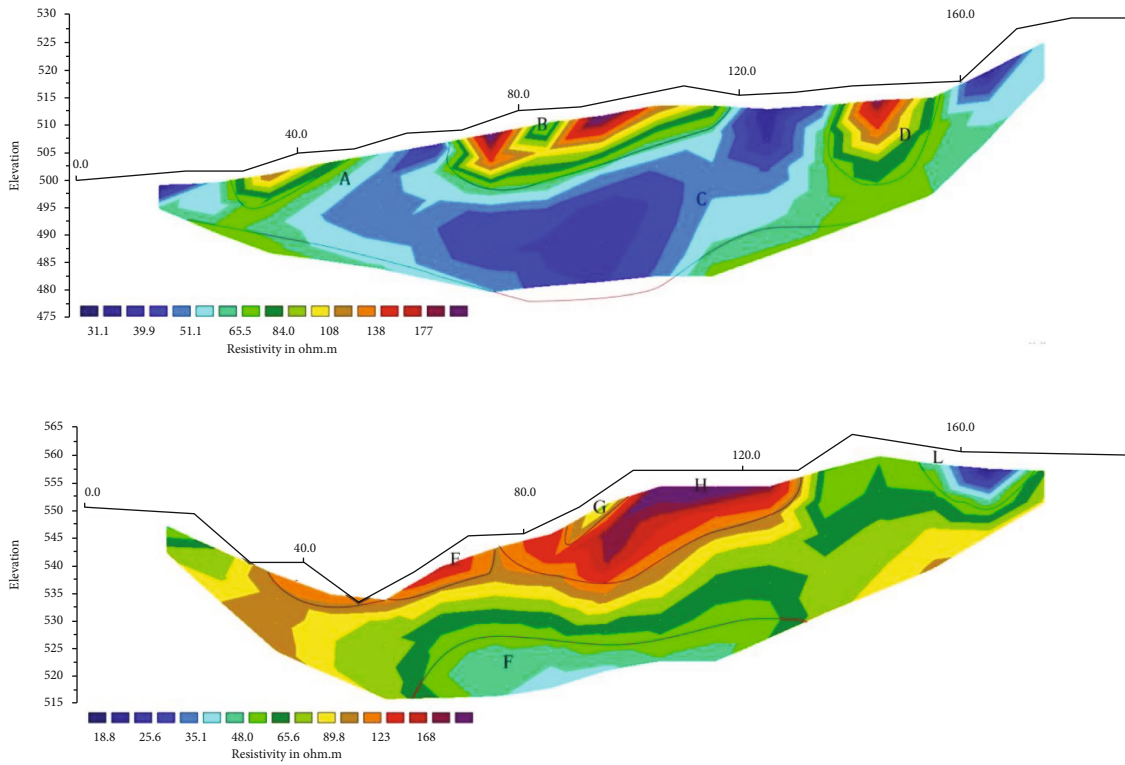
FIGURE 15: Measurement results in summer.

FIGURE 16: Measurement results in autumn.

4.4. Analysis of Inversion Results of Collected Field Data. To reflect the influence of rain in different seasons on the electrical characteristics of the underground structure, measure-ments were carried out in different seasons. This also aided in analyzing the development of underground structural fissures and the range affected by groundwater Artha and
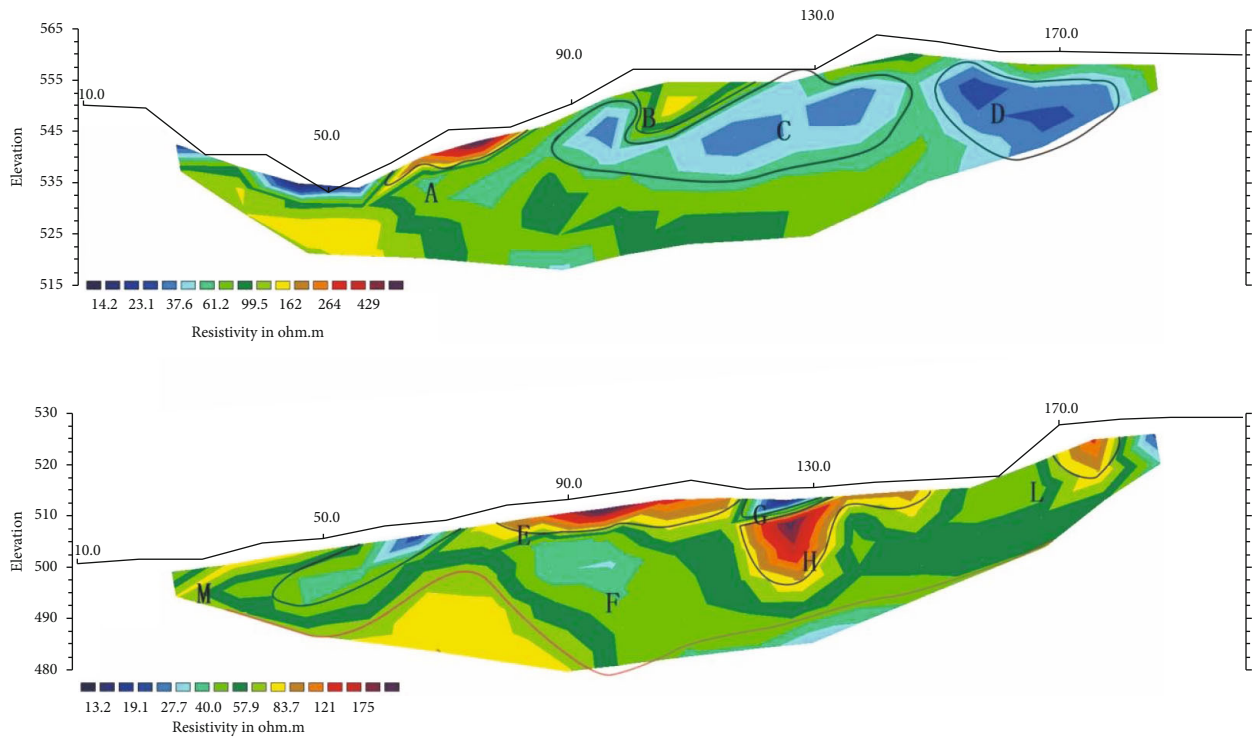
FIGURE 17: Measurement results in winter.

Julian [53]. The resistivity decreased significantly before and after rainfall, the area of low-resistivity anomaly increased by about 400 m^2, and the lowest resistivity decreased from 40 ($\Omega \cdot$m) to 25 ($\Omega \cdot$m). Smoothness constrained least square and unstructured grid-based finite element methods were applied to interpret the ERT data. The results show that the rate of change of the apparent resistivity in the shallow layer was low and that in the middle and deep layers was high. The upper picture of the measurement indicates the inversion result of the wiring along the slope (south to north). The lower picture indicates the inversion result of the wiring perpendicular to the slope direction (west to east).

Continuous rainfall is the primary cause of red bed landslides [26]. As shown in Figure 14, the field measurement date was February 2, 2021. In the above figure, D indicates the position where surface vegetation did not shift due to the large area of deeply buried high-resistivity rock mass, which prevented sliding in the area when the landslide occurred. C indicates the reservoir location. This area contained more water than the other areas of the formation. After the landslide, the water penetration was deeper, which resulted in a relatively low resistivity. B indicates the location of the east-side reservoir collapse (the depth is similar to the measured value). A indicates a small depression in the front of the slope. M indicates the area near the collapse of the back edge of the slope. E indicates the area where surface fissures developed on the south side of the slope, formed by the initial landslide. F and G indicate the locations of undisturbed strata. H and D correspond to locations of stable high-resistivity rock masses, and L indicates the location of cultivated land on the north side of the slope, which had a relatively low resistivity.

The field measurements were conducted on May 21, 2021. Evidently, with increased rainfall and improved underground hydrological conditions, as shown in Figure 15, the area of low-resistivity anomaly increased (A and C), area of high-resistivity anomaly decreased (B and D), and depth at C increased. This indicates that with increased rainfall, the underground fissure water and permeable formation water increased. The changes at C and D were more evident, indicating that the majority of fractures were developed there. The minimal change in the inversion results indicates that a small volume of rain has little effect on the underground structure in a vertical direction.

The field measurements were conducted on September 22, 2020. From Figure 16, it can be observed that A and C areas increased substantially and began to connect with each other. The abnormal range at B disappeared, and the high-resistivity body at D decreased substantially. As observed in Figure 14, B indicates the collapse section on the east side of the reservoir. Although rainfall increased the water content in the deep layers and decreased the resistivity, the collapse section of the surface layers still indicates a high-resistivity anomaly. Compared with Figure 14, the high-resistivity rock mass at D was more prominent, and the inference of stable non-sliding rock mass was more accurate, as observed in the figure on the right. The majority of the rock is hydrophilic, except for the stable high-resistivity rock at H, and as rock water content increased, the resistivity decreased. The resistivity of undisturbed strata at M was also reduced due to rainfall, indicating that the inversion results were reliable reference values.

The field measurements were taken on December 3, 2020. The measurement line was 150 m, and the other
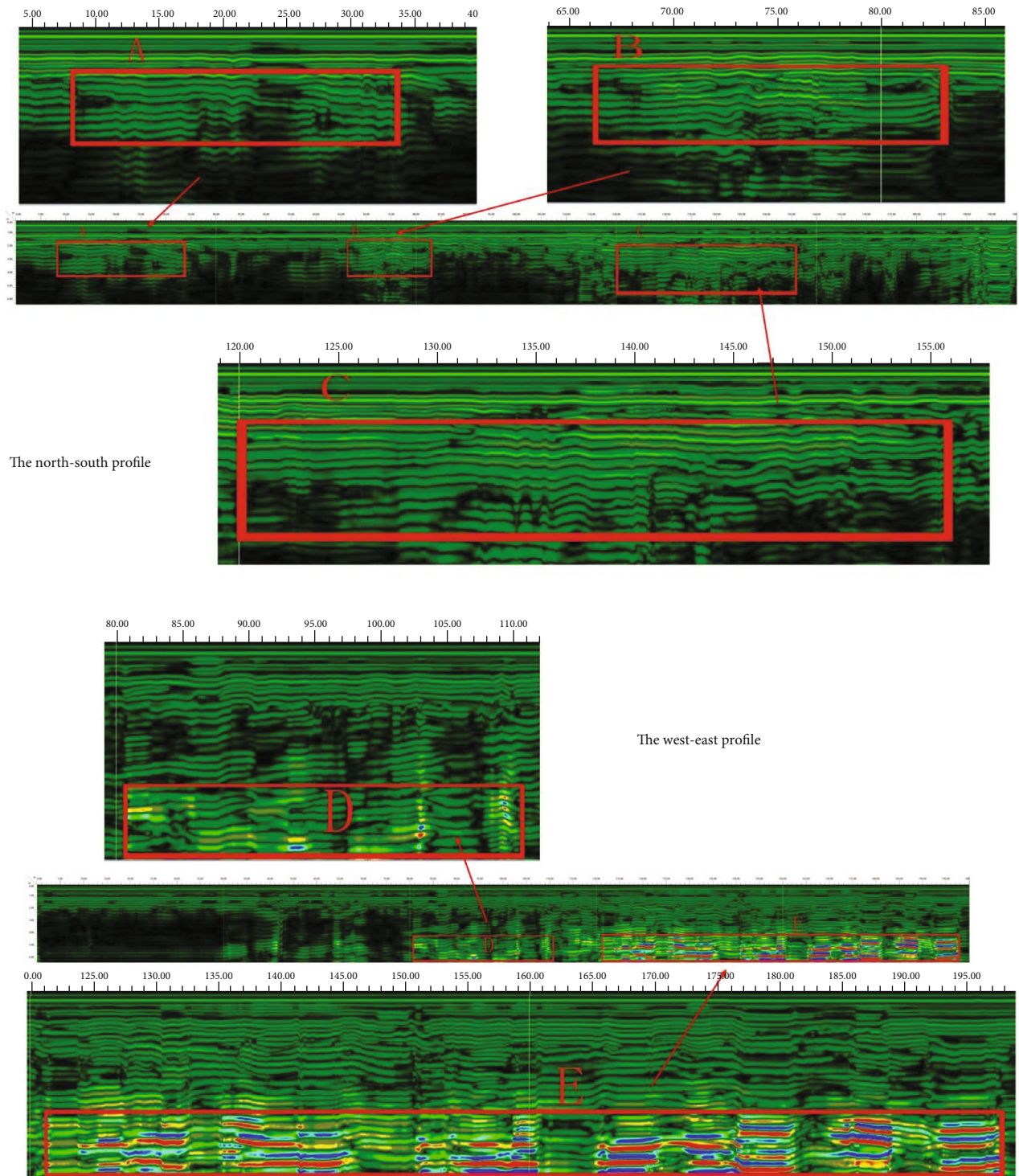
FIGURE 18: Ground penetrating radar results. The three abnormal areas A, B, and C in the west-east direction basically correspond to the three low-resistance abnormal areas near the surface of the autumn survey results, and the abnormal reflection points of D and E in the north-south direction basically correspond to the two low-resistance abnormal areas near the surface of the resistivity profile.

measurement lines were 200 m. As shown in Figure 17, the position of A remained largely consistent throughout the study period. Within these field measurements, the respective positions of C and D correspond to the position of C in

the other figures. Evidently, the decrease in groundwater level leads to a conspicuous decrease in the low-resistivity anomaly. The high-resistivity rock mass at H is highlighted. The resistance at F and L increased, and the entire formation
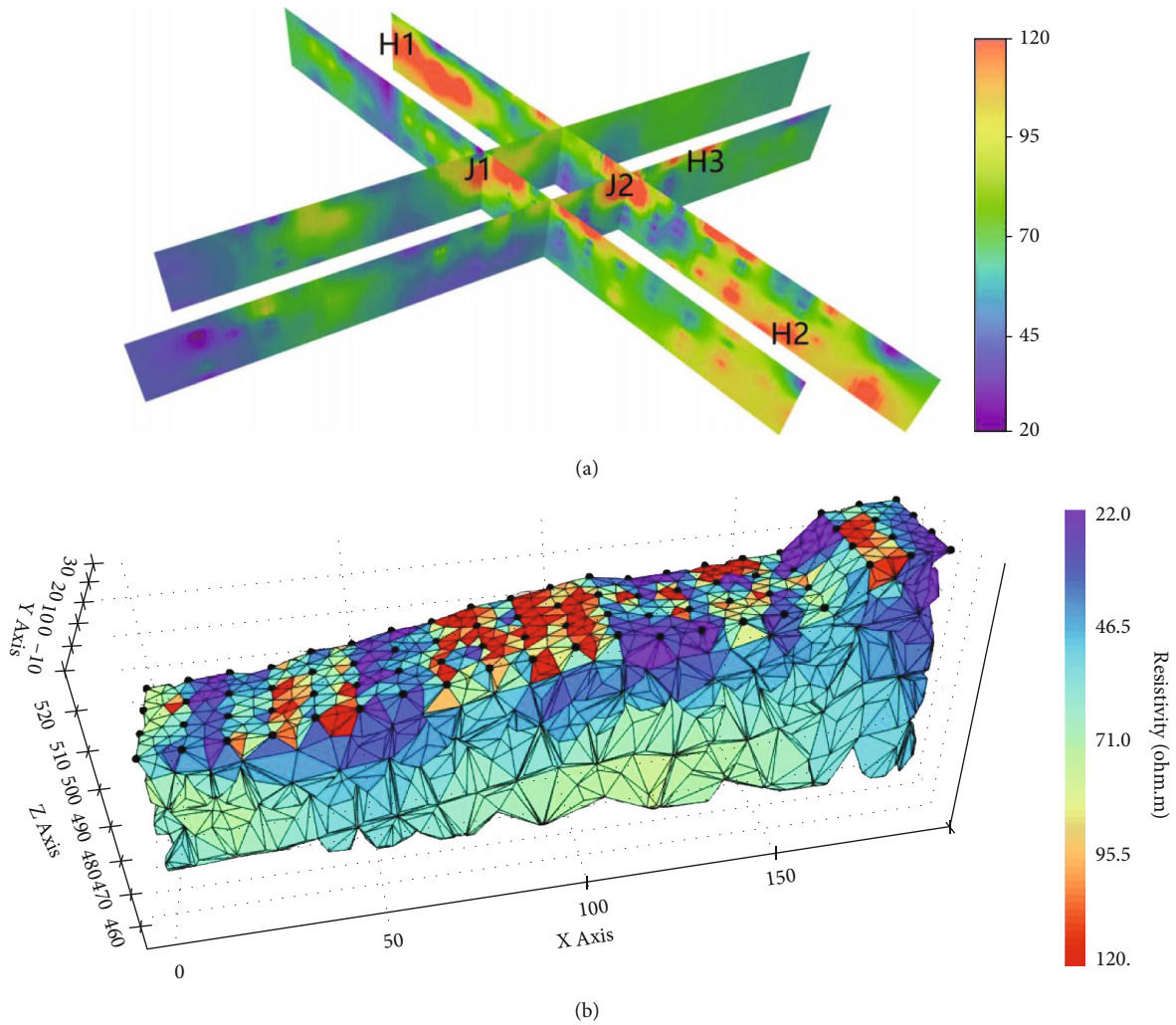
(a)

(b)

FIGURE 19: Three-dimensional electric resistivity tomography imaging. (a) shows J1 corresponds to the abnormal position of high resistivity of cross-section E and H; H1 largely corresponds to the position of M; H2 indicates the deep extension direction of H, showing high-resistivity anomaly. H3 shows the longitudinal section of the high resistivity of area D, that is, the area where the initial and secondary landslides did not move the hard rock mass. (b) shows the three-dimensional inversion results with grid lines, corresponding to the two-dimensional section, indicating the abnormal position of high-resistivity landslide mass. This is convenient for disaster evaluation and analysis.

FIGURE 20: The investigation on vegetation death. X shows the plants have died.
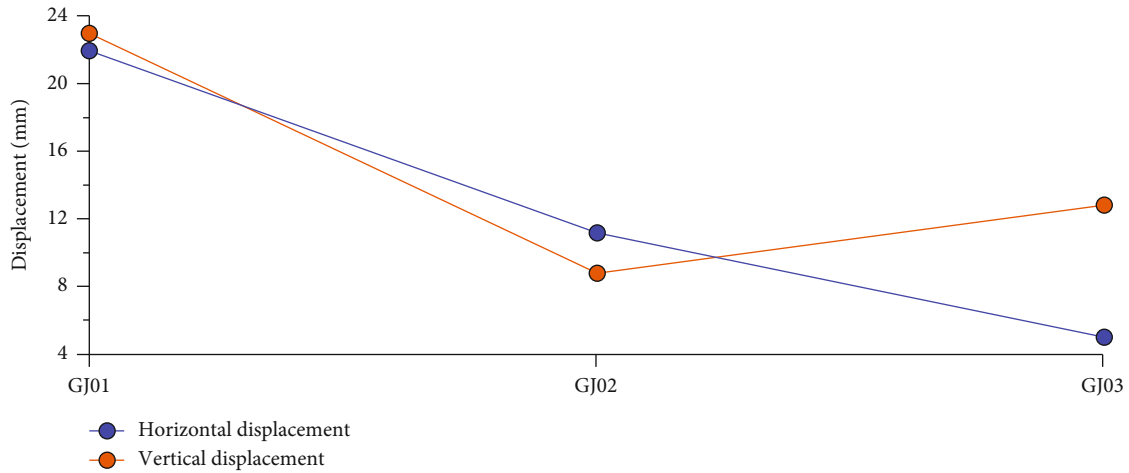
FIGURE 21: Electrical property anomaly and displacement of the surface monitoring station location.

TABLE 2: The landslide classification table (cite from [47]).

Type	Angle α	Name	Development model
			Unipolar translation
	$\alpha<10°$	Approximately horizontal slip surface landslides	Plate girder
			The multi-step translational
			Translational
	$10°<\alpha<30°$	Small dip landslide	Creep-crack type
			Rotation type
Rocks landslide			Slip-crack type
			Bent-split type
	$\alpha>30°$	General dip landslide	Slip-pressing-crack type
			Wedge block
			Compression-split type
	$10°<\alpha<30°$	Flat shallow landslide	Small dip slip shallow-crack type
Soil type landslide	$30°<\alpha<50°$	Thick-layer landslide	Circular arc accumulation layer creep fracture type

profile was largely maintained. Comparing the inversion results in autumn and winter better explains the structure of the underground space.

4.5. Ground Penetrating Radar.
Ground penetrating radar (GPR) is a geophysical method that uses the reflection of high-frequency electromagnetic waves to detect the target and geological structure. The frequency band of electromagnetic waves emitted by GPR is typically more than 107 Hz, and the wavelength of the GPR is generally 0.1–2 m in strata media [54]. GPR has a higher resolution than seismic methodology in detecting shallow strata media and can identify the structural characteristics of slope deposits and bedrock from the line and plane [55].

In this exploration, the energy attenuation of GPR in the gravel accumulation area was rapid, only reflecting in formation within a few meters. The results indicated that there were many inhomogeneous bodies on the surface of the landslide. The strong reflection areas of the radar image largely correspond to areas with a relatively abundant amount of water. As shown in Figure 18, the top image

shows the results of the survey line arranged along the land slide (south–north), whereas the bottom figure shows the results of the survey line arranged along the vertical slope (west–east). Evidently, the abnormal reflection points D and E in the west–east line correspond to two low-resistivity abnormal areas near the surface of the resistivity profile. Additionally, the three anomalous areas, namely, A, B, and C, in the west–east direction corresponded to the three low-resistivity anomaly areas near the surface of the autumn Moreover, GPR is economical, rapid, nondestructive, and easy to operate measurement result. The responses of the two methods to abnormal bodies were similar.

4.6. Three-Dimensional Imaging.
Several measuring lines were simultaneously arranged across the landslide mass. Each line had a function of electrical sounding. The lines intersected at fixed points, and three-dimensional mapping was conducted to show the differences in the spatial electrical characteristics of the landslide [56]. As shown in Figure 19, the north–south line indicates a relatively low resistivity, whereas the west–east line shows a relatively high
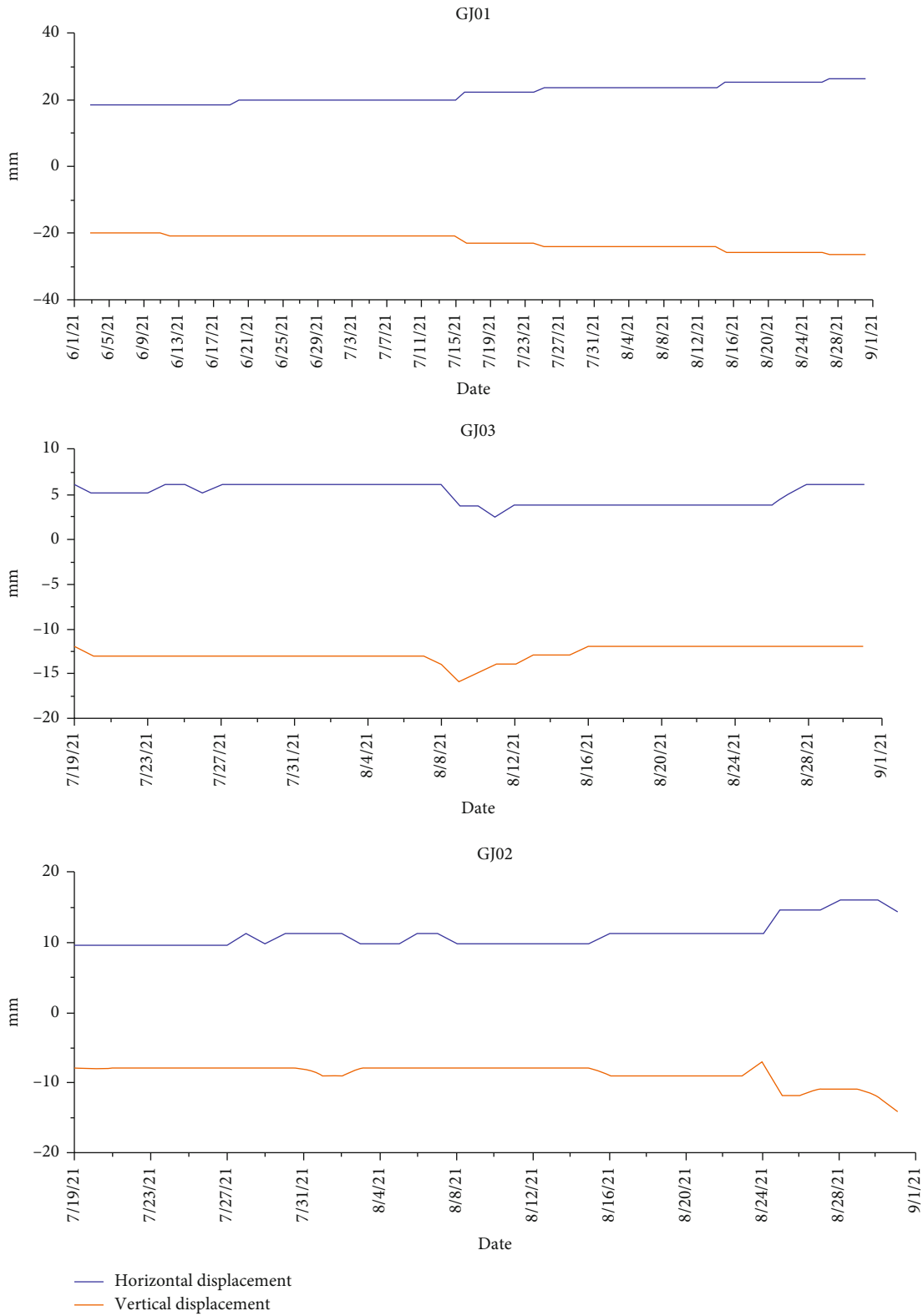
FIGURE 22: Geological Hazard Monitoring: Monitoring point GJ01 is at the rear edge of the landslide mass; monitoring point GJ02 is north of the landslide mass; monitoring point GJ03 is south of the middle of the landslide mass.

resistance. This is consistent with the results from the vertical and horizontal sections of the landslide from different seasons. J1 corresponds to the abnormal position of E and H high resistivity in the west-east section; H1 and M are basically in the same position; H2 is basically in the deep extension direction of H, showing a high-resistivity

FIGURE 23: Rainfall monitoring results.
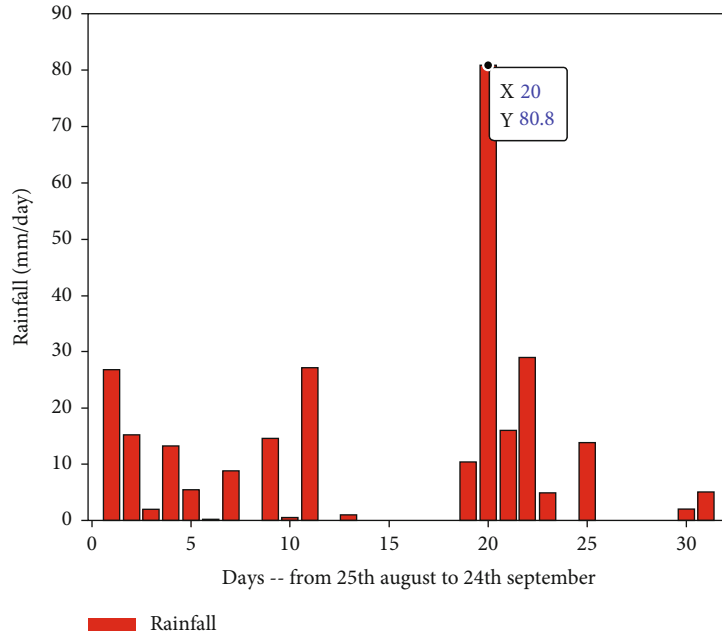

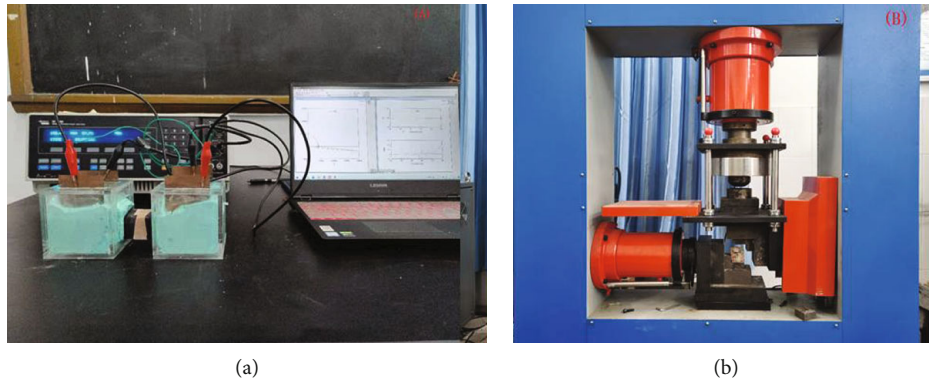(a)   (b)

FIGURE 24: The sample test in the lab. (a) is the measurement of electrical characteristic. (b) is the measurement of rock mechanical parameters.

TABLE 3: The resistivity measurements in the laboratory.

Number	Dry sample ($\rho(\Omega.m)$)	Wet sample ($\rho(\Omega.m)$)
1	508.76	39.9224
2	8.998	5.4032
3	0.0	0.0
4	1773.80	194.0035
5	294.4	15.48667
6	216.6	17.3406
7	438.4	18.19925
8	338.3	6.965927
9	1033.8	17.15245
10	689.8	6.122851
11	625.6	5.596332
12	491.9	5.116002
13	948.0	4.312442
14	641.5	5.23271

anomaly; H3 is the high resistance D in the north-south section, which is the hard rock mass where the secondary landslide and the primary landslide did not move.

5. Results and Discussion

5.1. Surface Vegetation Survey. After the landslide, the porosity and moisture content of soil change, which directly affects the growth of plants. As shown in Figure 20, the survival rate of surface vegetation on which plants are taller than 1.5 meters was investigated immediately one year after the landslide. Located in the middle of the Sichuan Basin with a humid climate, the landslide area was clothed with a thick growth of plants. In the vicinity of the landslide mass, there are approximately 215 plants (natural plants and artificially planted plants combined) taller than 1.5 meters, among which 78 have died, with a mortality rate close to 27.6%. Twenty-three plants taller than 4 meters were are recorded, of which 12 have died, with a mortality rate of
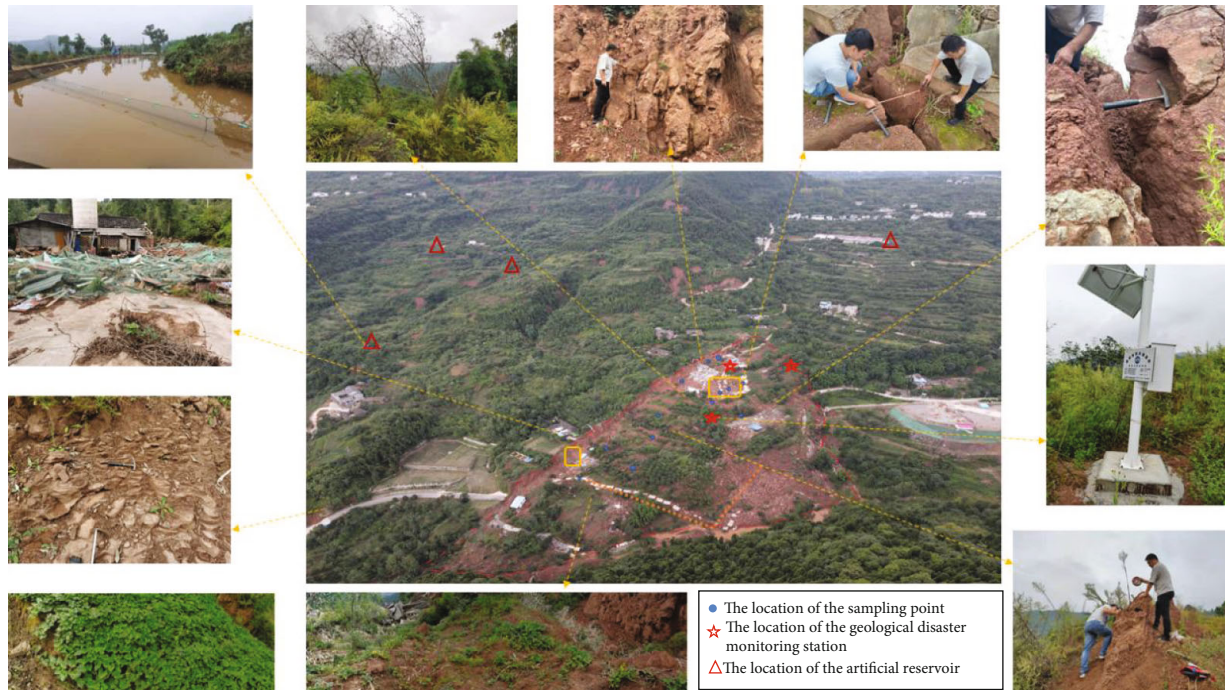
FIGURE 25: Comprehensive analysis of the landslide.

TABLE 4: Surface fissure changes after the occurrence of the landslide.

Time	Crack length	Crack width
November 2020	The maximum length is 13 cm	The maximum length is 12 cm
August 2021	The maximum length is 12 cm	The maximum length is 37 cm

more than 50%. At the same time, it can be seen in the lower right corner of Figure 21 that the artificially planted plants bore a heavy toll during the landslide. At the same location, the plants in the landslide-free area grew luxuriantly, while the growth of the vegetation on the landslide mass obviously did not. This phenomenon shows that after the landslide, the soil quality needs a long time to recover to the extent that plants can be planted.

As shown in Table 2, the growth of plants at different points of the landslide mass stands very much, in contrast to Figure 19. Generally, plants enjoy a higher rate of survival within the high-resistance abnormity area and a lower rate of survival within the low-resistance abnormity area [40]. The closer plants get to the rear edge of the landslide mass, the higher their survival rate is; the mortality rate from secondary slip is higher than that from the initial slip. Therefore, plants planted by human beings are more subject to death. However, precautionary measures can be taken because the growth of plants in the later stage of landslides can be predicted through 3D geophysical surveys.

5.2. Geological Hazard Monitoring. The location of the surface monitoring meter is shown in Figure 5, and the monitoring results are shown in Figure 22, from the horizontal and vertical displacement data of on-site geological disaster monitoring points, it can be seen that the horizontal and vertical displacements of monitoring point GJ01 near

the trailing edge of the landslide mass were basically stable. As the rainy season arrives, the displacement increases slightly, which indicates that after the landslide, the trailing edge of the landslide mass remains basically stable, and there will be a slight horizontal movement and vertical settlement if rainfall increases [48, 57]. The horizontal and vertical displacements of monitoring point GJ02 near the northern part of the landslide mass changed greatly, especially in late August, when the rainfall increased markedly. At that time, there was a sudden increase in both displacements, and the vertical displacement continued to rise at the initial stage. As the terrain at monitoring point GJ02 is steep, the surface damage is small in the presence of landslides, and the subsequent rainfall will cause further damage to the landslide mass, so if the rainfall increases, the stratum will be soaked and softened by rainwater. On August 23, 2021, a sharp rise in the horizontal displacement and in the vertical displacement due to collapse was recorded. In this connection, it can be said that there was a greater possibility of landslides again in the coming days. The horizontal and vertical displacements of monitoring point GJ03 near the south edge of the landslide mass were generally stable and only fluctuated before and after August 10, 2021, indicating that the middle part of the landslide mass was relatively stable after the landslide, with occasional occurrences of mild displacements.

TABLE 5: The growth of plants in electrical anomaly on the landslide mass.

(a)

High-resistance abnormality area		
	Artificial planted plants	Naturally growing plants
Total	50	28
Number of deaths	17	4
Mortality	34%	14.3%

(b)

Low-resistance abnormality area		
	Artificial planted plants	Naturally growing plants
Total	102	58
Number of deaths	54	15
Mortality	52.9%	25.9%

FIGURE 26: Important geographical location.

As shown in Figures 21 and 23, rainfall triggered the deformation of the landslide mass. In terms of the geophysics, the anomaly with a high resistance had a large displacement change, while the anomaly with a low resistance had a small displacement change. Through observation of the surface displacements and the utilization of the direct current, the upper fissure change and stability of the landslide will be accurately predicted.

5.3. Indoor Performance Test of Rock. As shown in Figure 24, (A) sample resistivity measurements were carried out using resistivity/conductivity meters in the laboratory. The measurement results are shown in Table 3. The resistivity values of the samples soaked in water are significantly reduced, and the resistance differences are obvious at different positions. (B) In the rock mechanics experiment, a total of 14 samples were taken at different locations within the range of the landslide mass. Since the measured results of every parame-

ter were basically the same, the average values of the measured parameters of the 14 samples were used in this study. The experimental results show that the friction force was 0.24 MPa; the friction angle was 32.47; the density was 1.96; the moisture content was 3%; and the porosity was 3%. The friction force of the rock in the study area was very small, the anti-sliding ability was relatively small, and the density was low, which triggers the formation of landslides.

5.4. Investigation and Analysis. According to the field investigation, there were two artificial reservoirs within the landslide mass in the study area, as shown in the yellow wireframe in Figure 25. In addition, there were four artificial reservoirs within 1 km of the landslide, and their locations are shown in the triangle in the figure. Early research shows that the existence of artificial reservoirs in the study area led to the occurrence of the secondary landslides. However, a large number of artificial reservoirs are dispersed in the

Longquan Mountain area, and their peripheral suspended heights range from 1.5 m to 3 m. Once geological disasters occur at reservoir locations, they can lead to more serious disasters [27]. Through the field investigation of the cracks in the whole landslide area, it was found that there were approximately 247 cracks with widths greater than 15 cm and lengths greater than 2 m, of which the cracks have a maximum crack length of 12 m and a maximum crack width of 37 cm (Table 4). Compared with Table 5, the strength of rock mechanical properties in the study area decreases sharply underwater immersion, which makes fractures develop. In addition, there are many crisscross cracks in the middle of the landslide mass, indicating that the landslide was triggered by multiple forces acting in different directions, which is consistent with the view that the landslide turns out to be a secondary landslide.

The investigation shows that the undisturbed stratum was horizontally layered, while the stratum in the south of the landslide mass had an inclination angle of approximately 31 degrees, and the stratum in the north had an inclination angle of approximately 42 degrees, which can explain the secondary damage caused by the secondary landslide and the steep terrain in the north. It can be seen in Figure 25 that the houses within 20 meters of the landslide mass were also damaged, indicating that the landslide produced strong vibrations, thereby destroying the houses outside the landslide. Comparing before and after the landslide, most exposed deposits collapsed, with an average collapse height of approximately 11 centimeters, indicating that they suffered serious weathering within one year, which is consistent with the mechanical properties of red-layer soft rocks in the Longquan Mountains, where the rocks are susceptible to softening, weathering, and low-intensity motion when exposed to water.

As shown in Figure 26, the landslide site has a special geographical location and it is very close to a scenic spot and important ecological area. The information derived from studying the causes of the landslide and its post-disaster impact can be directly applied to the disaster prevention and ecological environment protection construction of natural scenic spots.

After a landslide event, it is necessary to conduct landslide investigations and analyses to understand the failure mechanisms and the evolution model of the landslide. These insights also provide a better understanding of landslides, which is necessary for landslide prevention efforts [55, 58]. The present results offer insights into a specific landslide case study, provide a better understanding of landslides, and aim to prevent future geological hazards (Zhu et al. (2019)).

6. Conclusions

This study analyzed the development of the landslide, time effect of the landslide, and its impact on the human settlements in different seasons. On the basis of the geophysical survey, with the combination of the field hydrogeology, engineering geology, and rainfall, the following conclusions have been drawn.

(1) Through the surface investigation, it can be determined that the landslide can be divided into two areas, and the secondary landslide is mainly caused by the collapse of the pool. At the same time, the change of groundwater level caused by rainfall can be well reflected by geophysical means, and the main cause of sliding can be determined

(2) By comparing the results of ground investigation and geophysical exploration, it can be concluded that the landslide is mainly caused by heavy rainfall and human activities. The landslide process is divided into multiple stages, and the landslide continues to migrate after occurrence, and the surface plants are affected to a certain extent

(3) The spatial interpretation of the hydrogeological structure of the landslide mass by geophysical methods, combined with surface monitoring, is conducive to the interpretation and evaluation of the landslide occurrence process and its later impact on the environment from the spatial and internal structure

(4) The landslide is a typical Red Mudstone Landslide. It is of great significance for the investigation and geophysical monitoring of landslide through the red layer and provides a new idea for landslide disaster early warning and monitoring in mountainous areas of Sichuan Basin

Data Availability

The data are generated from experiments and can be available from the corresponding author upon request.

Conflicts of Interest

The authors declare that there are no conflicts of interest regarding the publication of this paper.

Acknowledgments

References

[1] N. Grima, D. Edwards, F. Edwards, D. Petley, and B. Fisher, "Landslides in the Andes: forests can provide cost-effective landslide regulation services," *Science of the Total Environment*, vol. 745, p. 141128, 2020.

[2] J. B. Peng, Z. J. Fan, D. Wu et al., "Heavy rainfall triggered loess-mudstone landslide and subsequent debris flow in Tianshui, China," *Engineering Geology*, vol. 186, pp. 79–90, 2015.

[3] Y. G. Zhang, Z. Zhang, S. Xue, R. Wang, and M. Xiao, "Stability analysis of a typical landslide mass in the Three Gorges Reservoir under varying reservoir water levels," *Environmental Earth Sciences*, vol. 79, no. 1, 2020.

[4] Z. Zhang, W. Gao, C. Zeng, X. Y. Tang, and J. Wu, "Evolution of the disintegration breakage of red-bed soft rock using a logistic regression model," *Transportation Geotechnics*, vol. 24, 2020.

[5] F. Gutiérrez, M. Parise, J. De Waele, and H. Jourde, "A review on natural and human-induced geohazards and impacts in karst," *Earth- Science Reviews*, vol. 138, pp. 61–88, 2014.

[6] D. Sun, D. Zhang, and X. Cheng, "Framework of national non-structural measures for flash flood disaster prevention in China," *Water (Switzerland)*, vol. 4, no. 1, pp. 272–282, 2012.

[7] Z. L. Zhang, T. Wang, S. R. Wu, H. M. Tang, and C. Y. Liang, "The role of seismic triggering in a deep-seated mudstone landslide, China: historical reconstruction and mechanism analysis," *Engineering Geology*, vol. 226, pp. 122–135, 2017.

[8] Y. Chen, L. Zhao, Y. Wang, Q. Jiang, and D. Qi, "Precipitation data and their uncertainty as input for rainfall-induced shallow landslide models," *Frontiers of Earth Science*, vol. 13, no. 4, pp. 695–704, 2019.

[9] Z. Zhong, A. Li, R. Deng et al., "Study on deformation mechanism of upper arch of red soft rock subgrade of high-speed railway," *Chinese Journal of Rock Mechanics and Engineering*, vol. 39, no. 363(2), pp. 116–129, 2020.

[10] X. Kang, A. Kokkinaki, C. Power et al., "Integrating deep learning-based data assimilation and hydrogeophysical data for improved monitoring of DNAPL source zones during remediation," *Journal of Hydrology*, vol. 601, article 126655, 2021.

[11] P. Ering and G. L. S. Babu, "Characterization of critical rainfall for slopes prone to rainfall-induced landslides," *Natural Hazards Review*, vol. 21, no. 3, article 06020003, 2020.

[12] H. Hong, J. Liu, D. T. Bui et al., "Landslide susceptibility mapping using J48 Decision Tree with AdaBoost, Bagging and Rotation Forest ensembles in the Guangchang area (China)," *Catena*, vol. 163, pp. 399–413, 2018.

[13] Z. Liu, X. He, and C. Zhou, "Influence mechanism of different flow patterns on the softening of red-bed soft rock," *Journal of Marine Science and Engineering*, vol. 7, no. 5, p. 155, 2019.

[14] S. Hang, H. Deng, and T. Deng, "Research on water-physical property of the red bed of Zhanghe formation in central Yunnan," *Prarl River*, vol. 39, no. 6, pp. 54–57, 2018.

[15] Z. Zhong, A. Li, and R. Deng, "Experimental study on the time-dependent swelling characteristics of red-bed mudstone in Central Sichuan," *Yanshilixue Yu Gongcheng Xuebao/Chinese Journal of Rock Mechanics and Engineering*, vol. 38, no. 1, pp. 76–86, 2019.

[16] C. Zhou, X. Yang, and Y. Liang, "Classification of red-bed rock mass structures and slope failure modes in South China," *Geosciences (Switzerland)*, vol. 9, no. 6, p. 273, 2019.

[17] C. Zhou, S. Huang, and Z. Liu, "The interface process and its dynamic model of red-bed soft rock softening," *Rock and Soil Mechanics*, vol. 40, no. 8, 2019.

[18] X. Xie, H. Chen, and X. Xiao, "Microstructure characteristics and softening mechanism of red-bed soft rock under water-rock interaction," *Journal of Engineering Geology*, vol. 27, no. 5, 2019.

[19] K. Huang, B. Kang, and F. Zha, *Disintegration Mechanism and Hydrogeochemical Processes of Red-Bed Soft Rock under Drying-Wetting Cycle*, 2021.

[20] M. Zhou, J. Li, and Z. Luo, "Impact of water-rock interaction on the pore structures of red-bed soft rock," *Scientific Reports*, vol. 11, no. 1, p. 7398, 2021.

[21] P.-A. Duvillard, F. Magnin, A. Revil et al., "Temperature distribution in a permafrost-affected rock ridge from conductivity and induced polarization tomography," *Geophysical Journal International*, vol. 225, no. 2, pp. 1207–1221, 2021.

[22] C. Ling, A. Revil, Y. Qi et al., "Application of the Mise-a-la-Masse method to detect the bottom leakage of water reservoirs," *Engineering Geology*, vol. 261, p. 105272, 2019.

[23] H. G. Liu, *Analysis of Red Bed Hydrogeological Structure in the Middle Section of Longquan Mountain*, Chengdu University of Technology, Chengdu City, 2019.

[24] H. Tang, J. Wasowski, and C. H. Juang, "Geohazards in the three Gorges Reservoir Area, China - lessons learned from decades of research," *Engineering Geology*, vol. 261, article 105267, 2019.

[25] L. Z. Wu, L. M. Zhang, Y. Zhou et al., "Theoretical analysis and model test for rainfall-induced shallow landslides in the red-bed area of Sichuan," *Bulletin of Engineering Geology and the Environment*, vol. 77, no. 4, pp. 1343–1353, 2018.

[26] W. P. Mu, X. Wu, C. Qian, and K. Wang, "Triggering mechanism and reactivation probability of loess-mudstone landslides induced by rainfall infiltration: a case study in Qinghai Province, Northwestern China," *Environmental Earth Sciences*, vol. 79, no. 1, p. 19, 2019.

[27] Y. Gao, R. Jiang, and X. Xu, "The pressure buildup well test analysis considering stress sensitivity effect for deepwater composite gas reservoir with high temperature and pressure," *Geofluids*, vol. 2021, 16 pages, 2021.

[28] L. F. Han, Y. S. Wang, X. X. Wang, Y. M. Sun, and J. F. Wu, "Experimental study on the timeliness of water rock interaction in Mesozoic red beds in Longquanshan area," *Hydrogeology and engineering geology*, vol. 36, no. 6, pp. 59–61, 2009.

[29] Y. Kanie, M. Yanagida, and T. Tanaka, "Mudstone landslide in the Zushi Formation of the Miura Group," *Journal of the Geological Society of Japan*, vol. 102, no. 8, pp. 762–764, 1996.

[30] T. Nielson, J. Bradford, J. Pierce, and M. Seyfried, "Soil structure and soil moisture dynamics inferred from time-lapse electrical resistivity tomography," *Catena*, vol. 207, article 105553, 2021.

[31] J. Li, J. Tong, C. Xia, B. X. Hu, H. Zhu, and R. Yang, "Numerical simulation and experimental study on farmland nitrogen loss to surface runoff in a raindrop driven process," *Journal of Hydrology*, vol. 549, pp. 754–758, 2017.

[32] J. B. Peng, Y. Q. Leng, X. H. Zhu, D. Wu, and X. Tong, "Development of a loess-mudstone landslide in a fault fracture zone," *Environmental Earth Sciences*, vol. 75, no. 8, p. 11, 2016.

[33] O. Hungr, S. Leroueil, and L. Picarelli, "The varnes classification of landslide types, an update," *Landslides*, vol. 11, no. 2, pp. 167–194, 2014.

[34] L. Chen, L. Mei, B. Zeng, K. Yin, D. P. Shrestha, and J. Du, "Failure probability assessment of landslides triggered by earthquakes and rainfall: a case study in Yadong County, Tibet, China," *Scientific reports*, vol. 10, no. 1, p. 16531, 2020.

[35] K. He, B. Liu, and X. Hu, "Preliminary reports of a catastrophic landslide occurred on August 21, 2020, in Hanyuan County, Sichuan Province, China," *Landslides*, vol. 18, no. 1, pp. 503–507, 2021.

[36] S. Segoni, L. Piciullo, and S. L. Gariano, "A review of the recent literature on rainfall thresholds for landslide occurrence," *Landslides*, vol. 15, no. 8, pp. 1483–1501, 2018.

[37] L. Sun, B. Ma, L. Pei, X. Zhang, and J. L. Zhou, "The relationship of human activities and rainfall-induced landslide and

debris flow hazards in Central China," *Natural Hazards*, vol. 107, no. 1, pp. 147–169, 2021.

[38] S. H. Zhou, Z. Y. Tian, H. G. Di, P. J. Guo, and L. L. Fu, "Investigation of a loess-mudstone landslide and the induced structural damage in a high-speed railway tunnel," *Bulletin of Engineering Geology and the Environment*, vol. 79, no. 5, pp. 2201–2212, 2020.

[39] W. Liu, F. P. Gan, W. Zhang, and L. Jia, "Application of geophysical prospecting to karst collapse in red bed area," *Progress in Geophysics*, vol. 30, no. 6, pp. 2923–2930, 2015.

[40] J. Dou, A. P. Yunus, D. Tien Bui et al., "Assessment of advanced random forest and decision tree algorithms for modeling rainfall-induced landslide susceptibility in the Izu-Oshima Volcanic Island, Japan," *Science of the Total Environment*, vol. 662, pp. 332–346, 2019.

[41] H. Hong, P. Tsangaratos, I. Ilia, C. Loupasakis, and Y. Wang, "Introducing a novel multi-layer perceptron network based on stochastic gradient descent optimized by a meta-heuristic algorithm for landslide susceptibility mapping," *Science of the Total Environment*, vol. 742, article 140549, 2020.

[42] W. H. Schulz, J. B. Smith, G. Wang, Y. Jiang, and J. J. Roering, "Clayey landslide initiation and acceleration strongly modulated by soil swelling," *Geophysical Research Letters*, vol. 45, no. 4, pp. 1888–1896, 2018.

[43] G. Han, Z. Yu, R. Liu, Q. Tang, X. Wang, and L. Song, "Influence of surface roughness on shear behaviors of rock joints under constant normal load and stiffness boundary conditions," *Natural Hazards*, vol. 112, no. 1, pp. 367–385, 2022.

[44] S. Li, Y. G. Zhang, M. Y. Cao, and Z. N. Wang, "Study on excavation sequence of pilot tunnels for a rectangular tunnel using numerical simulation and field monitoring method," *Rock Mechanics and Rock Engineering*, vol. 1, pp. 1–15, 2022.

[45] W. Chen, X. Xie, J. Wang et al., "A comparative study of logistic model tree, random forest, and classification and regression tree models for spatial prediction of landslide susceptibility," *Catena*, vol. 151, pp. 147–160, 2017.

[46] Y. G. Zhang, J. Tang, Y. M. Cheng et al., "Prediction of landslide displacement with dynamic features using intelligent approaches," *International Journal of Mining Science and Technology*, vol. 2, no. 1, pp. 1–11, 2022.

[47] X. J. Ma, Y. F. Zhang, L. J. C. Hou, J. M. Li, and J. Li, "Classification and formation mechanism of landslide in red-bed region," *Railway Construction*, vol. 2, pp. 75–78, 2021.

[48] X. G. Wang, B. Q. Lian, L. Kai, and L. Li, "Trigger mechanism of loess-mudstone landslides inferred from ring shear tests and numerical simulation," *Journal of Mountain Science*, vol. 18, no. 9, pp. 2412–2426, 2021.

[49] X. B. Yuan, B. Xiang, D. Zhao, and H. E. Yun-Yong, "Analysis of cause and treatment measures for a landslide in red mudstone in Guangyuan-Bazhong expressway," *The Chinese Journal of Geological Hazard and Control*, vol. 23, no. 3, 2012.

[50] X. Zhu, J. Peng, B. Liu, C. Jiang, and J. Guo, "Influence of textural properties on the failure mode and process of landslide dams," *Engineering Geology*, vol. 271, 2020.

[51] F. Li, H. Zhou, and H. Ge, "Electrical characteristics of different types of landslide bodies investigated by high-density electrical method," *Geophysical and Geochemical Exploration*, vol. 43, pp. 215–221, 2019.

[52] R. Valois, J. M. Vouillamoz, S. Lun, and L. Arnout, "Mapping groundwater reserves in northwestern Cambodia with the combined use of data from lithologs and time-domain-electromagnetic and magnetic-resonance soundings," *Hydrogeology Journal*, vol. 26, no. 4, pp. 1187–1200, 2018.

[53] Y. Artha and E. S. Julian, "Landslide early warning system prototype with GIS analysis indicates by soil movement and rainfall," in *IOP Conference Series: Earth and Environmental Science*, Institute of Physics Publishing, 2018.

[54] C. Warren, A. Giannopoulos, and I. Giannakis, "gprMax: open source software to simulate electromagnetic wave propagation for Ground Penetrating Radar," *Computer Physics Communications*, vol. 209, pp. 163–170, 2016.

[55] A. Othman, I. M. Ibraheem, H. Ghazala, H. Mesbah, and T. Dahlin, "Hydrogeophysical and hydrochemical characteristics of Pliocene groundwater aquifer at the area northwest El Sadat city, West Nile Delta, Egypt," *Journal of African Earth Sciences*, vol. 150, pp. 1–11, 2019.

[56] S. Zhang, L. Zhang, W. He, T. Ling, Z. Deng, and G. Fu, "Three-dimensional quantitative recognition of filler materials ahead of a tunnel face via time–energy density analysis of wavelet transforms," *Minerals*, vol. 12, no. 2, p. 234, 2022.

[57] H. Wu, G. Zhao, and S. Ma, "Failure behavior of horseshoe-shaped tunnel in hard rock under high stress: phenomenon and mechanisms," *Transactions of Nonferrous Metals Society of China*, vol. 32, no. 2, pp. 639–656, 2022.

[58] Y. Gao, B. Li, H. Gao, L. Chen, and Y. Wang, "Dynamic characteristics of high-elevation and long-runout landslides in the Emeishan basalt area: a case study of the Shuicheng "7.23"landslide in Guizhou, China," *Landslides*, vol. 17, no. 7, pp. 1663–1677, 2020.